ACS APPLIED MATERIALS & INTERFACES
Research Article
www.acsami.org

Combined Photothermal and Surface-Enhanced Raman Spectroscopy Effect from Spiky Noble Metal Nanoparticles Wrapped within Graphene-Polymer Layers: Using Layer-by-layer Modified Reduced Graphene Oxide as Reactive Precursors

Xiangming Li,[†] Yihe Zhang,*[,†] Yaling Wu,*[,‡] Yang Duan,[†] Xinglong Luan,[†] Qian Zhang,[†] and Qi An*[,†]

[†]School of Materials Science and Technology, China University of Geosciences, Beijing, 100083, China
[‡]School of Chemistry and Molecular Engineering, Peking University, Beijing, 100083, China

Supporting Information

ABSTRACT: To fabricate functionally integrated hybrid nanoparticles holds high importance in biomedical applications and is still a challenging task. In this study, we report the first reduced graphene oxide (rGO)-nobel metal hybrid particles that present simultaneously the photothermal and surface-enhanced Raman spectroscopy (SERS) effect from the inorganic part and drug loading, dispersibility, and controllability features from LbL polyelectrolyte multilayers. The hybrid particles where spiky noble metal particles were wrapped within rGO-polyelectrolyte layers were prepared by a facile and controllable method. rGO template modified using polyethylenimine (PEI) and poly(acrylic acid) (PAA) via layer-by-layer technology served as the reactive precursors, and the morphologies of the particles could be facilely controlled via controlling the number of bilayers around the rGO template. The hybrid particle presented low cytotoxicity. After loading doxorubicin hydrochloride, the particles effectively induced cell death, and photothermal treatment further decreased cell viability. rGO-Ag hybrid particles could be prepared similarly. We expect the reported method provides an effective strategy to prepare rGO-noble metal hybrid nanoparticles that find potential biomedical applications.

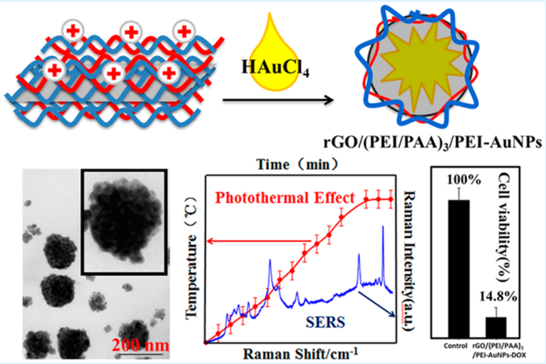

KEYWORDS: *hybrid nanoparticles, graphene, gold nanoparticles, photothermal, surface-enhanced Raman scattering, layer-by-layer*

1. INTRODUCTION

Hybrid functional nanoparticle complexes hold high potential in biomedical diagnostics and therapies. Specifically, noble metal nanoparticles have received intensive research interest and been universally studied in both theory and experiments due to their rich morphology-tunable surface plasmon resonance, signal enhancement abilities, and photothermal transition effect, etc.[1−8] Followed by the synthesis method proposed by Turkevich et al. in 1951 using citrate reduction,[9] the strategies to produce gold nanoparticles with various morphologies and thermal/optical properties have been largely enriched.[10,11] Equally important and versatile as nobel metal nanoparticles is the 2D carbon material the graphene family. Graphene oxide (GO) and reduced graphene oxide (rGO) have received especially intensive attention because of their chemical activities, electronic properties, photothermal effects in NIR range, and drug loading abilities.[12−23] The combination of nobel metal nanoparticles and graphene materials have further promoted the functionalities of the nanoparticles and achieved a higher level of versatility, being highly pursued in multiple applications including biomedical therapies.[24] Despite their appealing properties, the preparative strategies of the hybrid complex of nobel metal nanoparticles and graphene are still limited.[25] Spontaneous segregation of graphene oxide and nanoparticles lead to cargo-filled graphene nanosacks with multiple biomedical functions.[26−28] Post wrapping of gold nanorods led to effective cancer therapy agents with combined photothermal and chemotherapy efficacy as well as enhanced biocompatibility.[29,30] In order to achieve optimally integrated functions for the multifunctional particles, a lot of details should be carefully considered, including the stabilities in aqueous environment (dispersity), the morphological control of the nanoparticles, biotoxicity, and possibility to further functionalization by chemical reactions. Layer-by-layer (LbL) technique is a powerful method to establish biocompatible functional organic interfaces for various materials.[31] The technique of LbL assembly involves the alternate deposition of species with complementary chemical interactions and results in functional composite films. After decades of development, the LbL technique has grown into a well-defined method for the

Received: June 19, 2015
Accepted: August 13, 2015
Published: August 13, 2015

ACS Publications © 2015 American Chemical Society

DOI: 10.1021/acsami.5b05463
ACS Appl. Mater. Interfaces 2015, 7, 19353−19361

Scheme 1. (a) Layer-by-Layer Modification of rGO by PEI and PAA and (b) Polyelectrolyte Modified rGO Used As a Precursor to Produce and Wrap Spiky Noble Metal Nanoparticles

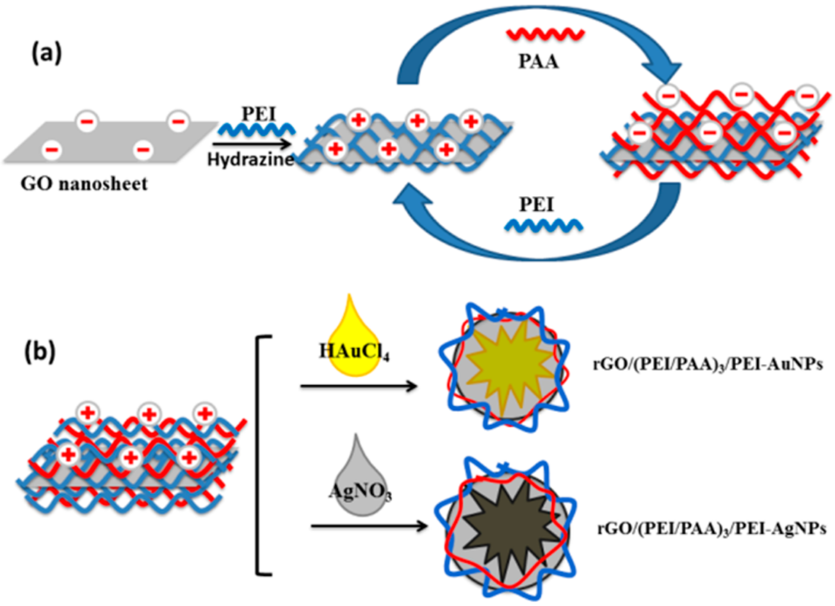

modification of interfaces and found applications in a wide variety of disciplines including biomaterials, drug delivery, engineering, electronics, diagnostics, and detection.[32−34] However, combined functionality of noble metal and graphene and dispersibility and controllability of LbL polyelectrolyte multilayers have not been integrated so far into a particulate complex.

In this report, we develop a controlled and facile method to prepare hybrid particulate complex of spiky noble metal nanoparticles and modified rGO. Layer-by-layer modification of polyelectrolyte around rGO core was first conducted to produce rGO precursors for the fabrication of the hybrid complexes. Upon adding $HAuCl_4$ but not any extraneous reducing agent, hybrid complexes of spiky noble metal nanoparticles (Au or Ag) wrapped by rGO was generated under sonication. The rGO-polyelectrolyte complex performed as the nanoreactor (ion enrichment matrixes with built-in reactivity), the reducing agent, the photothermal effective component, and the dispersers. Au or Ag particles thus generated presented spiky morphologies and showed an advantageous SERS effect. More interestingly, the control of the number of the polyelectrolyte bilayers around the rGO core provided fine kinetic control over the producing of the nanoparticles and results in multiple morphologies of the metal nanoparticles. The hybrid particle presented low cytotoxicity. After loading doxorubicin hydrochloride (DOX), the hybrid particles effectively induced cell death and photothermal treatment further decreased cell viability. The functionality and adaptivity of the reported method demonstrate the advantages of this strategy for producing the hybrid noble metal nanoparticles-rGO complex.

2. EXPERIMENTAL SECTION

2.1. Materials. Graphene oxide was purchased from XFNANO. Polyethylenimine (PEI) (700 kDa) and doxorubicin hydrochloride (DOX) were purchased from Aladdin. Poly(acrylic acid) (PAA) (100 kDa) was purchased from Alfa Aesar. Poly(allylamine hydrochloride) (PAH) (15 kDa) and Rhodamine B isothiocyanate were purchased from Sigma-Aldrich. Rhodamine 6G (Rh6G) were purchased from TCI (Shanghai) Development Co., Ltd. $HAuCl_4$ and sodium citrate were purchased from Sinopharm Chemical Reagent Beijing Co., Ltd. (Beijing, China). $AgNO_3$ was purchased from Xilong Co. Ltd., Beijing. Dulbecco's modified eagle medium was purchased from GIBCO.

2.2. LBL Assembly of rGO/(PEI/PAA)$_n$/PEI. Graphene oxide was sonicated for 2 h in water to form a stable dispersion. A volume of 20 mL of graphene oxide dispersion (0.25 mg/mL) was added dropwise (to avoid aggregation) to 20 mL of polyethylenimine (PEI) solution (5 mg/mL, pH 9.0) and stirred for 20 min. A volume of 15 μL of hydrazine hydrate (80%) was then added into the above-prepared solution to reduce GO. The mixed solution was heated and kept at 80 °C for 2 h. The resultant rGO/PEI was centrifuged (10 000 rpm for 20 min) and washed with deionized water for three times. The LbL assembly of polyelectrolyte around the rGO/PEI substrate was conducted as follows. rGO/PEI was dispersed into 20 mL of deionized water. The dispersion was added dropwise (to avoid aggregation) into 20 mL of poly(acrylic acid) (PAA) solution (5 mg/mL, pH 3.8) with stirring and kept stirring for 20 min. The resulting rGO/PEI/PAA was centrifuged (10 000 r/min) and washed by deionized water three times to remove extra PAA. The product was in turn modified with PEI in a similar manner, until the desired number of layers of polyelectrolyte was obtained around the rGO template (see Scheme 1).

2.2.1. Synthesis of PAH-RhB. In total, 50 mg of poly(allylamine hydrochloride) (PAH) was added into 0.1 M, pH 8.5 carbonate buffer and stirred at the same time. Then Rhodamine B (RhB) solution (in methanol) was added dropwise into the solution for 24 h. The resulting mixture was dialyzed with deionized water for 2 days and then the mixture was freeze-dried.

2.3. Preparation of rGO/(PEI/PAA)$_n$/PEI-AuNPs and rGO/(PEI/PAA)$_n$/PEI-AgNPs. The rGO/(PEI/PAA)$_n$/PEI-AuNPs were prepared by a simple one-pot method. In a typical recipe, 500 μL of $HAuCl_4$ (10 mM) was added dropwise to 1 mL of the rGO/(PEI/PAA)$_n$/PEI dispersion under sonication for 15 min. The mixture was then kept for another 3 days under ambient conditions. The method described above also applied to the preparation of rGO/(PEI/PAA)$_n$/PEI-AgNPs, using a $AgNO_3$ (10 mM) instead of the $HAuCl_4$ solution. The preparation of rGO/(PEI/PAA)$_3$/PEI-AuNPs with different concentrations of rGO/(PEI/PAA)$_3$/PEI solution or $HAuCl_4 \cdot 3H_2O$ was achieved similarly and the detailed recipe are provided in the Supporting Information.

2.4. Measurement of Photothermal Performance. The rGO/(PEI/PAA)$_3$/PEI-AuNPs solution was irradiated using NIR light (940 nm, power density 1.0 W/cm^2) for 15 min and the temperature of the

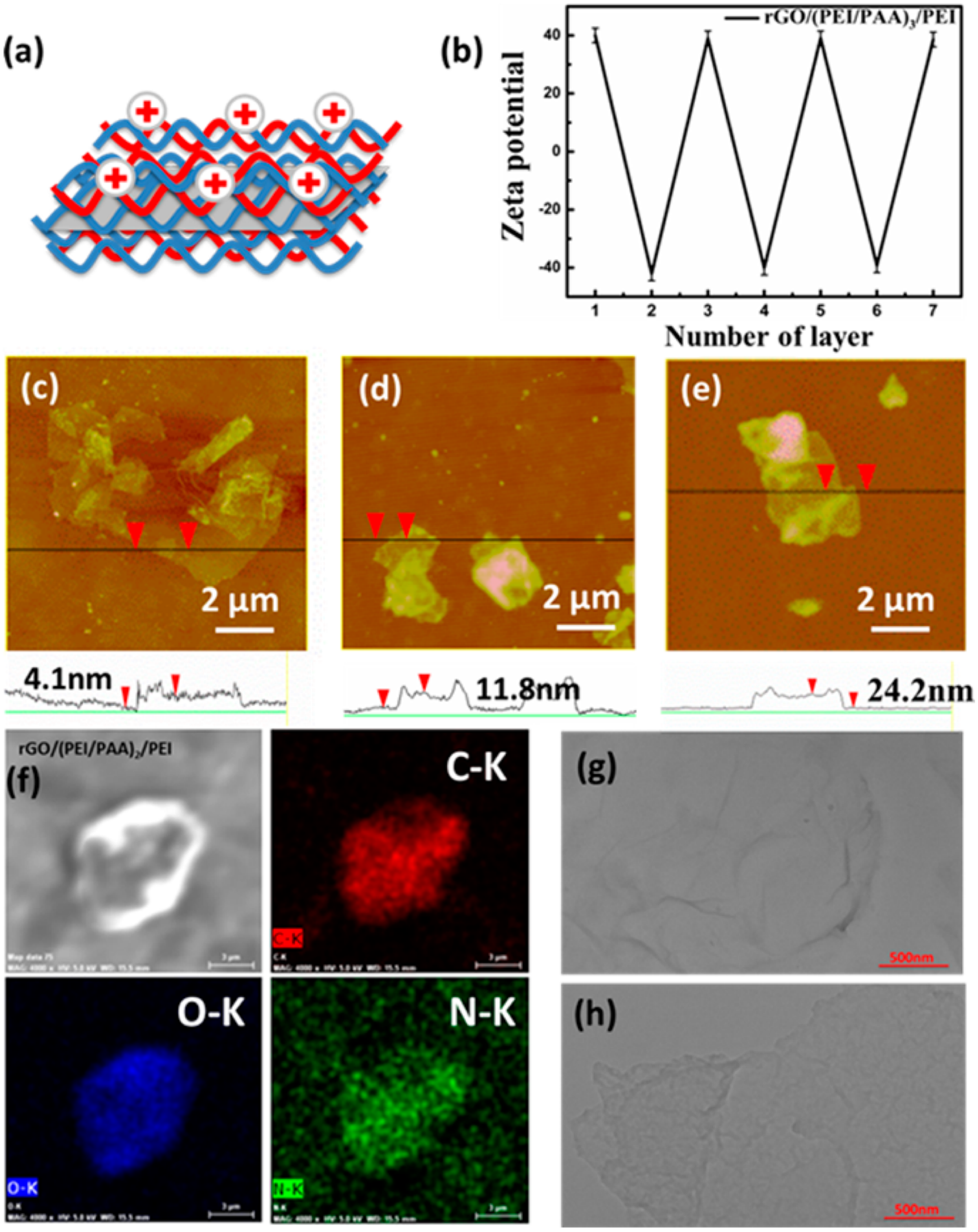

Figure 1. (a) Schematic illustration of rGO/(PEI/PAA)$_n$/PEI, (b) zeta potential of rGO/(PEI/PAA)$_n$/PEI during the assembly process. AFM images and height prolife of (c) rGO/PEI, (d) rGO/(PEI/PAA)$_2$, and (e) rGO/(PEI/PAA)$_3$/PEI. (f) Elemental mapping of the rGO/(PEI/PAA)$_2$/PEI. TEM images of (g) rGO/PEI and (h) rGO/(PEI/PAA)$_3$/PEI.

solution was measured every minute. The Au nanoparticles (AuNPs) reduced by sodium borohydride[35] and the rGO/(PEI/PAA)$_3$/PEI dispersions were used as control groups.

2.5. SERS Measurement. The rGO/(PEI/PAA)$_3$/PEI-AuNPs (or rGO/(PEI/PAA)$_2$/PEI-AgNPs) dispersions were dispersed in a solution of 1×10^{-6} M Rh6G or 1×10^{-4} M DOX by a volume ratio of 1:1. The mixed solution was kept for 1 h and then added dropwise onto a silicon substrate and dried for Raman characterization.

2.6. Drug (DOX) Loading. The rGO/(PEI/PAA)$_3$/PEI-AuNPs dispersions were mixed with DOX solution (the concentration of the aqueous DOX solution was 0.25 mg/mL) by a volume ratio of 1:2 for 24 h. The drug-loaded particles were washed for 3 times with deionized water by centrifugation (8000 rpm for 5 min) to remove free doxorubicin.

2.7. Cytotoxicity. The cytotoxicity of rGO/(PEI/PAA)$_3$/PEI-AuNPs and rGO/(PEI/PAA)$_3$/PEI-AuNPs-DOX toward Hela cells was measured by MTT assay. Logarithmically growing Hela cells were seeded at a density of 2.5×10^4 cells/well into 96-well plates and allowed to adhere for 24 h at 37 °C. Then the supernatant was replaced by 200 μL of culture medium supplemented with 10 μL/20 μL of rGO/(PEI/PAA)$_3$/PEI-AuNPs dispersions (using 0.25 mg/mL rGO/(PEI/PAA)$_3$/PEI dispersions as reactive precursors) and 10 μL/20 μL of rGO/(PEI/PAA)$_3$/PEI-AuNPs-DOX dispersions for 48 h. At the end of the treatment, the tetrazolium salt (MTT) was added to each well to a final concentration of 0.5 mg/mL and kept for 4 h. After removal of the medium, 150 μL of dimethyl sulfoxide was added and the mixture was incubated at 37 °C for 20 min to dissolve the formazan product. Then, the absorbance at 490 nm was measured with a microplate reader (Multiskan Mk3; Thermo Labsystems, Vantaa, Finland). Cell viability were calculated from the absorbance at 490 nm and were presented as a percentage of control values.

2.8. Characterization. Fourier transform infrared spectra (FTIR) were obtained with a PerkinElmer Spectrum 100. X-ray diffraction (XRD) was applied (Rigaku D/max-rA) to identify the crystalline-

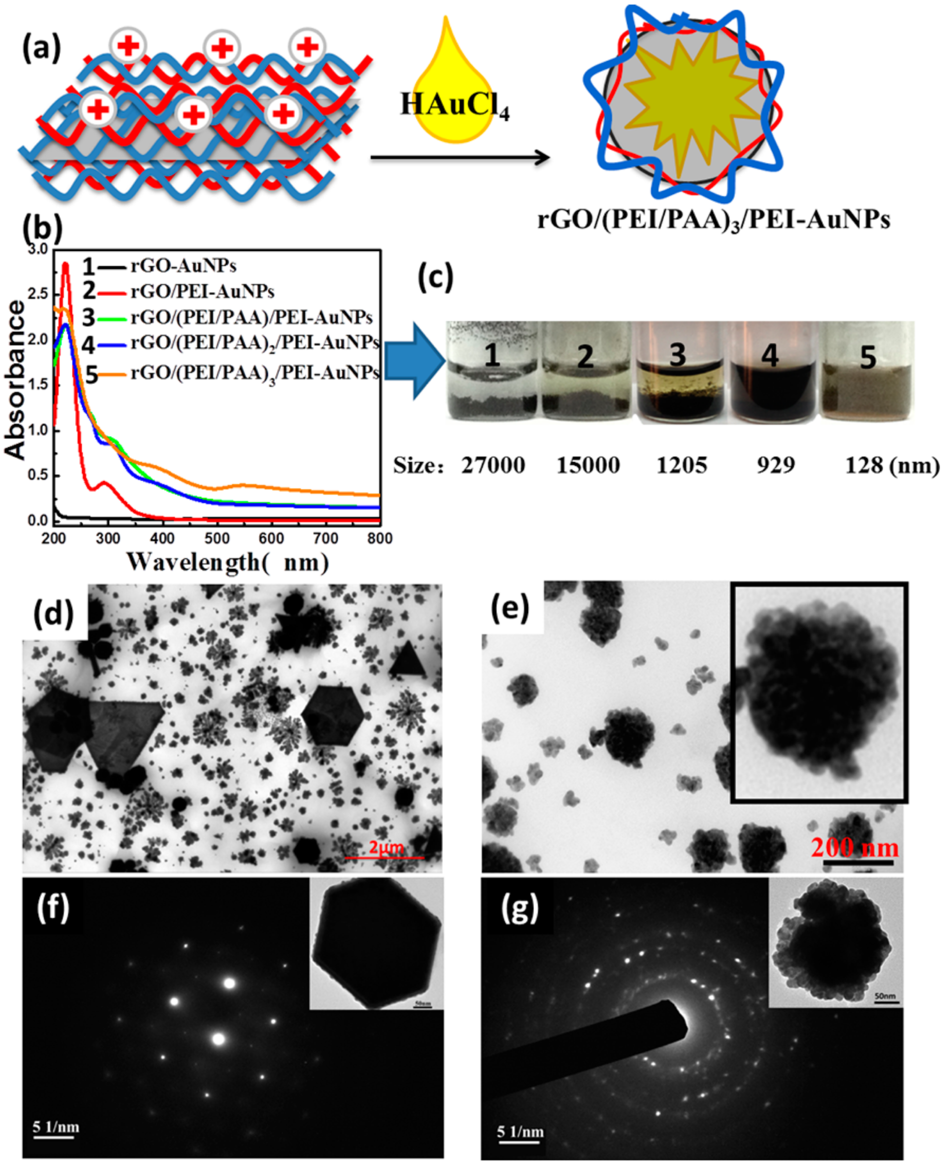

Figure 2. (a) Schematic illustration of using rGO/(PEI/PAA)$_n$/PEI as reactive precursors to prepare rGO/(PEI/PAA)$_n$/PEI-AuNP hybrid complexes. (b) UV−vis spectra of rGO-AuNPs and rGO/(PEI/PAA)$_n$/PEI-AuNPs with $n = 0−3$. (c) Optical images of dispersions of rGO-AuNPs and rGO/(PEI/PAA)$_n$/PEI-AuNPs with $n = 0−3$. TEM images of (d) rGO/(PEI/PAA)$_2$/PEI-AuNPs and (e) rGO/(PEI/PAA)$_3$/PEI-AuNPs. The inset in panel e is a zoom-in image of a hybrid complex particle. SAED patterns of (f) rGO/(PEI/PAA)$_2$/PEI-Au nanoplate and (g) rGO/(PEI/PAA)$_3$/PEI-AuNPs. Inset in panels f and g are TEM images of the corresponding particles.

phase structures. The elemental distribution was probed with scanning electron microscopy (SEM; SU1510, Hitachi Ltd., Tokyo, Japan), equipped with energy-dispersive spectrometry (EDS). Transmission electron micrographs (TEM, H-8100, Hitachi) were recorded using FEI TECNAI G2 20 transmission electron microscopy. The thickness and surface morphologies of rGO-polyelectrolyte complex nanosheet was obtained using atomic force microscopy (AFM, Dimension 3100) from Veeco, U.S.A. The zeta potential and size distribution of the hybrid particles were measured on a Malvern Instruments Zetasizer Nano-ZS90. The ultraviolet−visible (UV−vis) spectra were measured on an UV6100 double beam spectrophotometer. The samples for SERS test were recorded on a micro-Raman spectrometer (HORIBA, LabRAM HR Evolution) with 532 nm laser excitation.

3. RESULTS AND DISCUSSION

3.1. Characterization of rGO/(PEI/PAA)$_n$/PEI. The successful assembly of the multilayered polyelectrolyte films around rGO template in layer-by-layer fashions was confirmed by zeta potential, elemental mapping, and FTIR. The rGO-polyelectrolyte composite presented alternately positive and negative potentials around +40.0 mV and −40.0 mV, respectively, up to 3.5 bilayers (Figure 1a) (further assembly cycles not measured), indicating that the positively charged PEI and negatively charged PAA were assembled around the rGO template alternatively. Elemental mapping of rGO-(PEI/PAA)$_2$/PEI (Figure 1f) presented evenly distributed false color corresponding to C, O, and N on the substrate surface, indicating the even distribution and full coverage of the polyelectrolytes around the rGO template. FTIR further confirmed the successful assembly of PEI and PAA around rGO (Figure S1b). The vibrations of aromatic C=C (1552 cm^{-1}) and epoxy C−O (1195 cm^{-1}) were observed for rGO samples. After the LbL modification by PEI/PAA multilayers, a set of new peaks appeared. The vibrational band around 3400 cm^{-1} corresponded to hydroxyl and amine groups. Peaks at

1561 cm^{-1} corresponding to COO− groups verified the existence of PAA. Peaks corresponding to the C−N bond at 1476, 1291, and 1105 cm^{-1} indicated that PEI was assembled into the complex.[36] rGO-(PEI/PAA)$_3$/PEI remained with quasi-2D-morphology (Figure 1h) but presented increased thickness compared to rGO-PEI nanosheets (Figure 1g) as indicated by increased contrast between the sample and the background in TEM images. The accurate thickness of rGO-(PEI/PAA)$_3$/PEI was measured by AFM as 24.2 nm in contrast to 11.8 and 4.1 nm for rGO-(PEI/PAA)$_2$ and rGO-PEI (Figure 1c−e). The morphological measurements confirmed that polyelectrolyte PEI and PAA were assembled around the rGO core and indicated that the resultant complex nanosheets dispersed nicely with minimal aggregations. UV−vis spectra showed absorbance around 270 nm for rGO-(PEI/PAA)$_3$/PEI complex, which is characteristic of rGO (Figure S1a).

3.2. Preparation of rGO/(PEI/PAA)$_n$/PEI-AuNPs.

rGO/(PEI/PAA)$_n$/PEI-AuNP complex was achieved by adding aqueous solutions of HAuCl$_4$ into rGO/(PEI/PAA)$_n$/PEI (n = 0,1,2,3) colloid dispersions under ultrasonification (Figure 2a). The rGO/(PEI/PAA)$_n$/PEI complex served as both the reducing and dispersing agents. No external reducing agent was needed in this process. An absorbance band around 520 nm quickly emerged upon adding HAlCl$_4$ solution into the rGO/(PEI/PAA)$_n$/PEI complex dispersions, indicating the creation of AuNPs. The absorbance curve differed with the increase of value of n, indicating that AuNPs with distinct morphologies were generated by varying the number of bilayers in the rGO-polyelectrolyte complexes (Figure 2b). In accordance with the UV−vis spectra, an interesting observation from DLS results was that the dimensions of the complex reduced significantly with the increase of the number of bilayers around rGO cores. Comprehensive analysis based on FTIR, XRD, and Raman measurements demonstrated that the component of Au, PEI, PAA, and rGO coexisted in the obtained hybrid particles (Figures S2a and S3a).

The process of the generation of rGO/(PEI/PAA)$_n$/PEI-AuNP complex was explained as follows. The amines in PEI were positively charged after protonation and thus were able to absorb the chloroaurate anion (AuCl$_4^-$).[37,38] At the same time, PEI provided the reducing power for the generation of AuNPs from chloroaurate anions (Figure S4). Since the LbL multilayer was already assembled around the rGO core, with the in situ formation of the AuNPs in or near the polyelectrolyte multilayers, the rGO/(PEI/PAA)$_n$/PEI-AuNP hybrid complex was simultaneously obtained. This process also explains the phenomena that increasing the number of bilayers around the rGO core decreased the sizes of the rGO/(PEI/PAA)$_n$/PEI-AuNP hybrid complex. With the increase of the number of the bilayers, a larger amount of Au(III) was able to be held and enriched in the multilayers,[37] and denser reducing power was provided by more PEI species. Since the generation of AuNPs proceeds via a slow nucleation step followed by fast growth, enrichment of a larger amount of chloroaurate anion by increasing the number of bilayers, which in turn provided larger reducing power, would result in the formation of a larger amount of nuclei, which then quickly lead to the formation of a larger amount of AuNPs but of smaller sizes.[37] The adjustability of the morphologies of the hybrid complex highlighted the advantage of this synthesis strategy where local enrichment and embedded reducing power were integrated.

With the decrease of the sizes of the hybrid complex, the stabilities of their aqueous dispersions increased (Figure 2c). The enhanced stability might result from the balance of gravity which induces aggregation and the electrostatic repulsion and Brownian oscillation which promote dispersion. The morphological changes of the hybrid complex with the increase of the number of bilayers from 2.5 to 3.5 were also observed in TEM images (Figure 2d,e). The rGO/(PEI/PAA)$_2$/PEI-AuNP complex displayed diameters of around 1.5 μm with a mixture of shapes including spiky dendrimeric particles (13%), spiky spheres (84.4%), and Au sheets (2.6%), and 64% of these particles presented sizes within 100−500 nm. The large Au particles in this mixture could be partially removed by precipitation by keeping the mixture still for 3 days, and TEM images of the supernatant indicated that only small hybrid spiky particles of around 300 nm were left in the solution (Figure S5). In contrast, the rGO/(PEI/PAA)$_3$/PEI-AuNP complex presented dimensions of around 100 nm (32% within 100−200 nm and 68% within 50−100 nm) with mulberry-like shapes. Enlarged image of the rGO/(PEI/PAA)$_3$/PEI-AuNP complex indicated that the outermost layer of the complex around the Au core was composed of materials with weaker contrast in TEM view, consistent with the proposed image that the AuNPs were wrapped up by the rGO/(PEI/PAA)$_3$/PEI complexes. The existence of rGO/(PEI/PAA)$_3$/PEI complexes around the AuNP cores will be further confirmed by Raman spectra as discussed later. HR-TEM images of the rGO/(PEI/PAA)$_3$/PEI-AuNP complex are displayed in Figure S6, and the lattice parameter therein (0.235 nm) corresponded to Au 111 lattice. SEAD in Figure 2f,g clearly indicated that both the Au nanoplate and the Au spiky hybrid particles were crystalline but the orientation of the crystal plane differed when they sit on TEM copper grids. These results demonstrate that the preparation conditions and the precursors used influenced the morphologies of the resultant hybrid particles.

Further studies employing different preparative conditions of the hybrid complex demonstrated that the concentration of HAuCl$_4$ or rGO/(PEI/PAA)$_3$/PEI precursors influenced the ultimate morphologies of the rGO/(PEI/PAA)$_3$/PEI-AuNP hybrid complex (Figures S7 and S8). Enhanced concentrations of HAuCl$_4$ led to rapid formation of a larger amount of hybrid complex sheets with larger dimensions approaching 5 μm. Increased concentration of rGO/(PEI/PAA)$_3$/PEI resulted in more of a spherical product and fewer sheets and decreased particulate dimensions of the hybrid complex. The similar trend presented with higher concentrations of HAuCl$_4$ and lower concentrations of rGO/(PEI/PAA)$_3$/PEI demonstrated further that the formation of the hybrid complex was a competing process between nucleation and particulate growth. Faster nucleation provided by the larger ratio of rGO/(PEI/PAA)$_3$/PEI:HAuCl$_4$ resulted in a larger number of nuclei and smaller particulate dimensions and vice versa.[35,36]

The growth (or ripeness) process of the complex was revealed in further detail by monitoring the evolvement of the particulate morphologies over time (Figure S9). The reaction rate was decreased by concomitantly decreasing the concentrations of rGO/(PEI/PAA)$_3$/PEI and HAuCl$_4$ to half of the original value to allow the time-dependent observation by TEM and UV−vis spectra. Particles of around 100 nm with darker cores and less dark peripheries existed in day 1. At this moment, the onset of the coalescence of the core area was observable in TEM images (Figure S9). In day 7, only large particles of around 800 nm of irregular shapes existed. SAED pattern indicated samples in day 7 presented well-defined

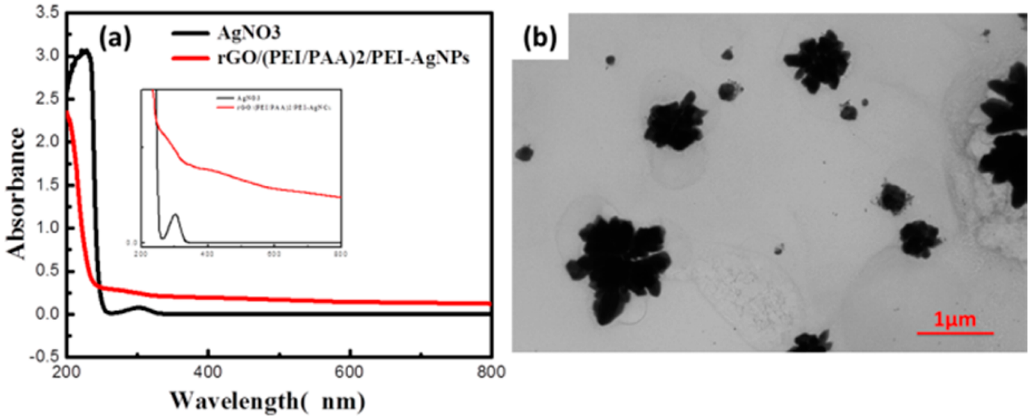

Figure 3. (a) UV−vis spectra of rGO/(PEI/PAA)$_2$/PEI-AgNPs and an enlarged view, (b) TEM image of the rGO/(PEI/PAA)$_2$/PEI-AgNPs.

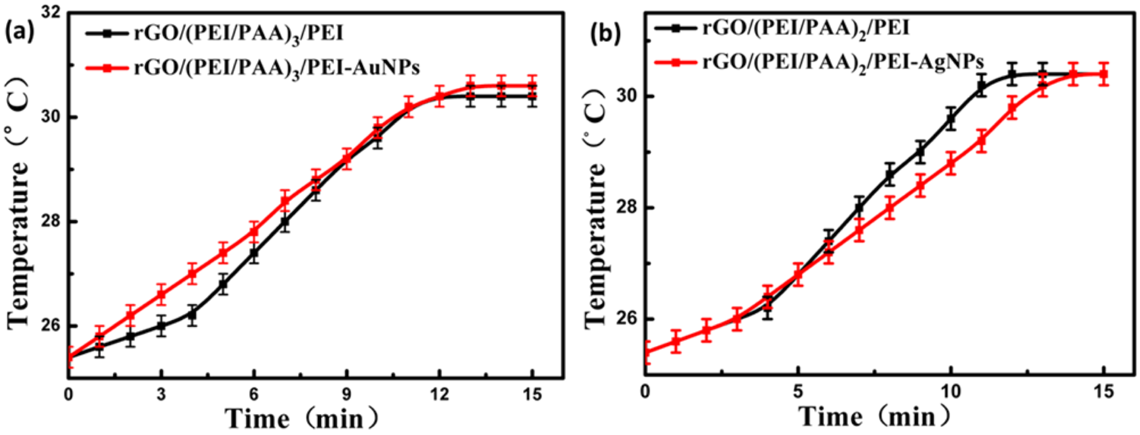

Figure 4. Photothermal performance of (a) rGO/(PEI/PAA)$_3$/PEI-AuNPs and (b) rGO/(PEI/PAA)$_2$/PEI-AgNPs.

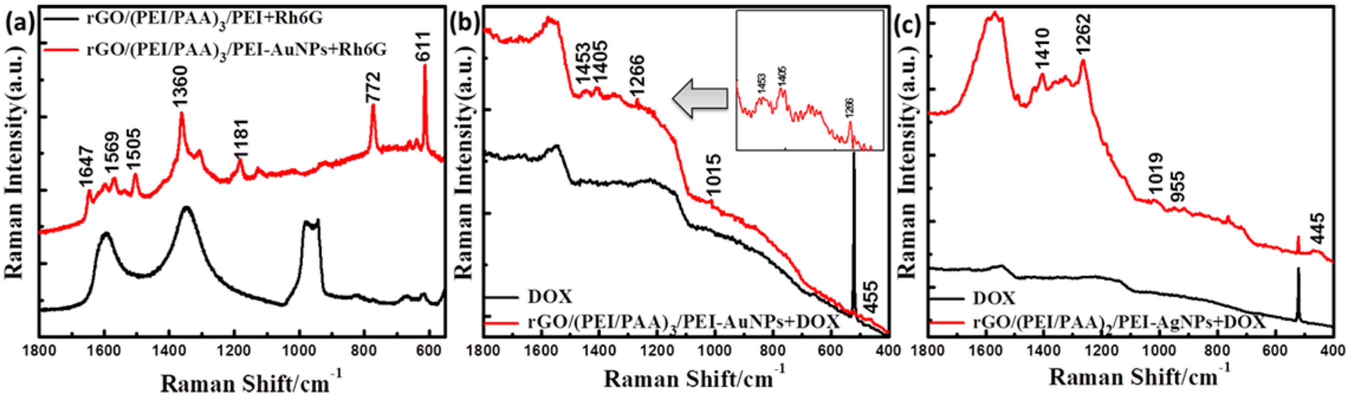

Figure 5. SERS of (a) rGO/(PEI/PAA)$_3$/PEI-AuNPs+Rh6G, (b) rGO/(PEI/PAA)$_3$/PEI-AuNPs+DOX, and (c) rGO/(PEI/PAA)$_2$/PEI-AgNPs +DOX. The concentration of Rh6G is 10^{-6} M. The concentration of DOX is 10^{-4} M.

crystalline structure. Corresponding to the morphological changes of the complex observed by TEM, the UV−vis spectra also changed over time. Samples in day 1 only displayed characteristic absorbance of rGO (∼270 nm) and $HAuCl_4$ (300−400 nm). In day 3, a characteristic plasmonic band corresponding to AuNP appeared, and the intensity of the band further increased until day 7. These results indicated that the ripening of the complex can last for several days and coalescence of complex took place in this process. The particles in this observation prepared using smaller precursor concentrations displayed larger dimensions, indicating that the morphologies of the complex was kinetically controlled and slow growth lead to larger particles.

The preparative strategy was also applied to produce Ag complex to demonstrate generality of the method. Both UV−vis spectra and TEM images demonstrated the successful preparation of rGO/(PEI/PAA)$_2$/PEI-AgNP hybrid complex (Figure 3). In the UV−vis spectra, the distinction of the characteristic absorbance of $AgNO_3$ at around 210−220 nm and the emergence of a new absorbance band at around 420 nm suggested the formation of the Ag complex. TEM images indicated that the Ag complex was of spiky dendritic shapes with lateral dimensions ranging from around 300 nm to larger

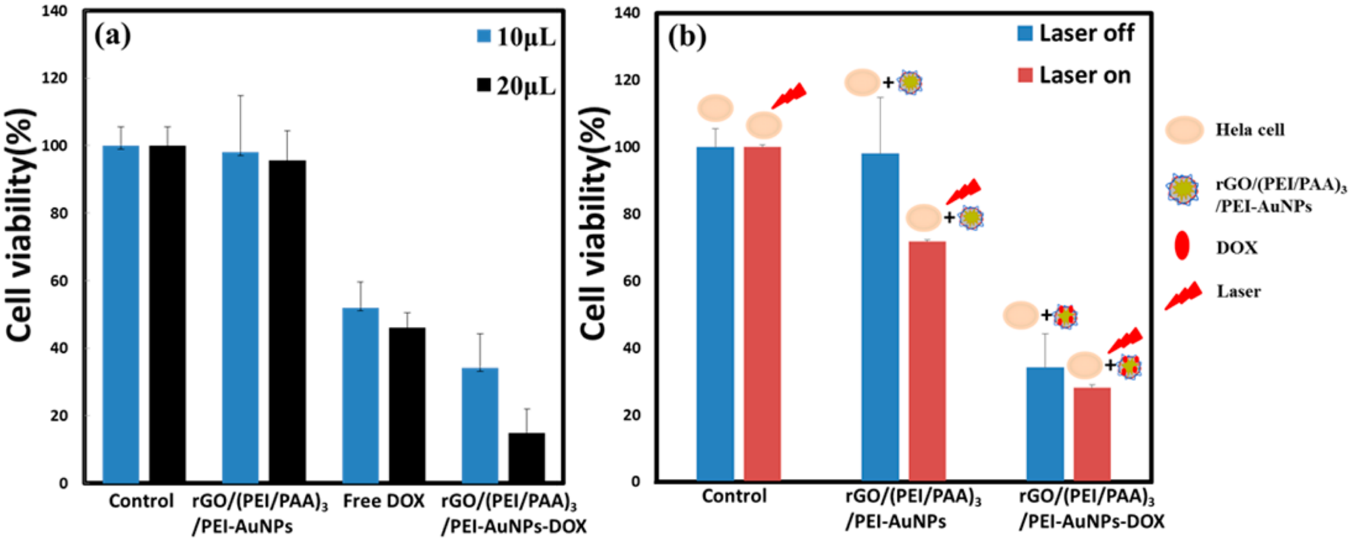

Figure 6. (a) MTT assay of HeLa cells incubated with 10 μL/20 μL of rGO/(PEI/PAA)$_3$/PEI-AuNPs, 10 μL/20 μL of free DOX, and 10 μL/20 μL of rGO/(PEI/PAA)$_3$/PEI-AuNPs-DOX, (b) MTT assay of HeLa cells incubated with 10 μL of rGO/(PEI/PAA)$_3$/PEI-AuNPs or 10 μL of rGO/(PEI/PAA)$_3$/PEI-AuNPs-DOX with and without NIR irradiation.

than 1 μm. FT-IR and XRD confirmed that PEI, PAA, rGO, and Ag coexisted in these particles (Figures S2b and S3b).

3.3. Photothermal Performance of rGO/(PEI/PAA)$_3$/PEI-AuNPs and rGO/(PEI/PAA)$_2$/PEI-AgNPs. The rGO/(PEI/PAA)$_3$/PEI-AuNP hybrid complex presented remarkable photothermal effect, obviously superior to that of AuNPs prepared using citrate acid as the reducing and protecting agent. Upon IR irradiation, the temperature of the rGO/(PEI/PAA)$_3$/PEI-AuNPs dispersion (Figure 4a) increased from 25.4 to 31.0 °C while the temperature of the AuNPs dispersions (Figure S10) were essentially unchanged within 15 min. The temperature of the rGO/(PEI/PAA)$_2$/PEI-AgNPs solution (Figure 4b) also increased from 25.4 to 30.4 °C upon IR irradiation. The temperature rise of out hybrid particle dispersions were comparable to the temperature change of the rGO dispersions upon IR irradiation, indicating that our hybrid particles presented effective photothermal effects, which were mainly contributed by the rGO component therein. It is worth noting that the small temperature change resulting from the small laser power used in this study should be preferable to avoid tissue damage but did not indicate that the photothermal effect was inferior, since the cell apoptosis was reported to be induced by a local temperature change around the particles and the possibly generated active species.[39−41]

3.4. SERS of rGO/(PEI/PAA)$_3$/PEI-AuNPs and rGO/(PEI/PAA)$_2$/PEI-AgNPs. The complex also displayed the advantageous SERS effect. Rh6G was frequently used as a SERS reporter to indicate the effectiveness of the SERS effect in previous studies.[42−45] So we also chose Rh6G to indicate the enhancement effect of our hybrid particles. Rh6G in solution (10^{-6} M) could be detected by our hybrid complex (Figure 5a). This low concentration could not be directly detected by Raman spectra without the enhancement effect: the characteristic vibrational features of Rh6G was absent for the [rGO/(PEI/PAA)$_3$/PEI + Rh6G] sample, and only Raman scattering for graphene materials (1360 cm^{-1} and 1590 cm^{-1}) were observed. In comparison, after processing using our rGO/(PEI/PAA)$_3$/PEI-AuNPs complex, obvious Raman scattering features corresponding to Rh6G (1569, 1505, 1181, 772, and 611 cm^{-1}) were obtained. The detection limit of 1×10^{-6} M of Rh6G was comparable to previously reported noble-metal particles or rGO-noble metal particle hybrid sheets[42−44] but was superior to rGO-wrapped-nobel metal hybrid particulate spheres.[45] rGO/(PEI/PAA)$_3$/PEI-AuNPs displayed the best SERS effect compared with rGO/(PEI/PAA)$_1$/PEI-AuNPs or rGO/(PEI/PAA)$_2$/PEI-AuNPs complex. The enhanced Raman scattering effect was presumed from both molecular accumulation effect of rGO multilayers and enhancement effect of the mulberry-shaped gold clusters. Characteristic scattering corresponding to rGO at 1360 cm^{-1}, and 1590 cm^{-1} were also observed for the Rh6G-loaded hybrid particles. The signal enhancement effect of our hybrid particles could be further used to indicate drug loading to the particles. After loaded with DOX, SERS characteristic of DOX were clearly presented by rGO/(PEI/PAA)$_3$/PEI-AuNPs or rGO/(PEI/PAA)$_2$/PEI-AgNPs at 455, 1015, 1266, 1405, and 1453 cm^{-1} (Figure 5b,c). In a further step, we attached RhB onto polyaromatic hydrocarbon (PAH) polymeric chains and incorporated it into the rGO/(PEI/PAA)$_3$/PAH-RhB-AuNPs complex. Raman signals from RhB could also be detected (Figure S11), suggesting that the complex could also be potentially used as self-reporting tracers. rGO/(PEI/PAA)$_2$/PEI-AgNPs also displayed an effective SERS effect, and 10^{-6} M of Rh6G in solution could be clearly detected (Figure S12).

3.5. Cell Toxicity and Combined Chemo-Phototherapy Effect. The rGO/(PEI/PAA)$_3$/PEI-AuNPs and rGO/(PEI/PAA)$_2$/PEI-AgNPs complex were stable in cell culturing media for at least 3 days[46] (Figure S14) and presented low cytotoxicity (Figure 6 and Figure S15). After incubation in cultures containing the rGO/(PEI/PAA)$_3$/PEI-AuNPs complex (20 μL) for 48 h, cell viability remained higher than 97%, as measured by MTT. Because of the proper size of the Au complex for the enhanced permeability and retention (EPR) effect, we further tested the possibility to use them as therapy agents. DOX could be loaded into the rGO/(PEI/PAA)$_3$/PEI-AuNPs complex effectively as indicated by UV−vis absorbance (Figure S13b). The loading efficiency was 0.0423 mg/mL and the loaded DOX was released by passive diffusion which lasted for 5 h. HeLa Cell viability decreased to 14.8% for cells cultivated in medium containing the drug-loaded rGO/(PEI/

PAA)$_3$/PEI-AuNPs complex. IR irradiation did not influence cell viability when the photothermal reagent rGO/(PEI/PAA)$_3$/PEI-AuNPs was absent. However, with the presence of rGO/(PEI/PAA)$_3$/PEI-AuNPs, cell viability decreased to 70% after IR irradiation for 15 min. Combined therapy effects toward HeLa cell were observed by applying both the DOX-loaded complex and IR irradiation. Cell viability decreased to 33% upon adding the DOX-loaded complex (half the dosage in previous experiments), and a further decrease of cell viability to 26% was observed when IR irradiation was further introduced. These results indicated our complex could be used as combined chemical and photothermal therapy agent and tumor cells could be effectively terminated using our complex particles. Free DOX was also able to cause cell apoptosis but less effective than our loaded hybrid particles at the same concentration.

■ CONCLUSION

In this report, we have developed a rapid, stable, and controllable method to synthesize rGO-gold hybrid nanoparticles. The prepared hybrid particles presented simultaneously photothermal and SERS effect and were able to load drug molecules. rGO template modified by polymeric species using the LbL method served as the reactive precursors of the rGO-Au hybrid nanoparticles. The morphologies of the hybrid particles were controllable via controlling the number of bilayers around the rGO template. The method could also be used to prepare rGO-Ag hybrid particles. The particles presented low cytotoxicity. While after loading with DOX, the complex with AuNPs effectively induced cell death, and the photothermal treatment further decreased cell viability. We expect the reported method serve as an effective strategy to prepare rGO-noble metal hybrid nanoparticles with organic interfaces that find potential biomedical applications.

■ ASSOCIATED CONTENT

Ⓢ Supporting Information

The Supporting Information is available free of charge on the ACS Publications website at DOI: 10.1021/acsami.5b05463.

> UV−vis, FTIR spectra, TEM images, and XRD patterns of the complex particles and cell toxicity of the complex particles (PDF)

■ AUTHOR INFORMATION

Corresponding Authors

*E-mail: zyh@cugb.edu.cn.
*E-mail: wylleg@163.com.
*E-mail: an@cugb.edu.cn.

Notes

The authors declare no competing financial interest.

■ ACKNOWLEDGMENTS

This work was supported by the NSFC (Grant 21303169), the Fundamental Research Funds for the Central Universities (Grants 2652013115, 35532015002), Beijing Nova Program (Grant Z141103001814064), Beijing Specific Project to Foster Elitist (Grant 2013D009015000001), and National High Technology Research and Development Program of China (863 Program Grant 2012AA06A109), and the special coconstruction project of Beijing City Education.

■ REFERENCES

(1) Guerrero-Martínez, A.; Grzelczak, M.; Liz-Marzán, L. M. Molecular Thinking for Nanoplasmonic Design. *ACS Nano* **2012**, *6*, 3655−3662.

(2) Kelly, K. L.; Coronado, E.; Zhao, L. L.; Schatz, G. C. The Optical Properties of Metal Nanoparticles: The Influence of Size, Shape, and Dielectric Environment. *J. Phys. Chem. B* **2003**, *107*, 668−677.

(3) Pallavicini, P.; Taglietti, A.; Dacarro, G.; Diaz-Fernandez, Y. A.; Galli, M.; Grisoli, P.; Patrini, M.; Santucci De Magistris, G.; Zanoni, R. Self-Assembled Monolayers of Silver Nanoparticles Firmly Grafted on Glass Surfaces: Low Ag^+ Release for an Efficient Antibacterial Activity. *J. Colloid Interface Sci.* **2010**, *350*, 110−116.

(4) Daniel, M.-C.; Astruc, D. Gold Nanoparticles: Assembly, Supramolecular Chemistry, Quantum-Size-Related Properties, and Applications toward Biology, Catalysis, and Nanotechnology. *Chem. Rev.* **2004**, *104*, 293−346.

(5) Halas, N. J.; Lal, S.; Chang, W.-S.; Link, S.; Nordlander, P. Plasmons in Strongly Coupled Metallic Nanostructures. *Chem. Rev.* **2011**, *111*, 3913−3961.

(6) Romo-Herrera, J. M.; Alvarez-Puebla, R. A.; Liz-Marzán, L. M. Controlled Assembly of Plasmonic Colloidal Nanoparticle Clusters. *Nanoscale* **2011**, *3*, 1304−1315.

(7) Dykman, L.; Khlebtsov, N. Gold Nanoparticles in Biomedical Applications: Recent Advances and Perspectives. *Chem. Soc. Rev.* **2012**, *41*, 2256−2282.

(8) Ghosh, P.; Han, G.; De, M.; Kim, C. K.; Rotello, V. M. Gold Nanoparticles in Delivery Applications. *Adv. Drug Delivery Rev.* **2008**, *60*, 1307−1315.

(9) Turkevich, J.; Stevenson, P. C.; Hillier, J. *Discuss. Faraday Soc.* **1951**, *11*, 55−75.

(10) Brust, M.; Walker, M.; Bethell, D.; Schiffrin, D. J.; Whyman, R. Synthesis of Thiol-derivatised Gold Nanoparticles in a Two-phase Liquid-Liquid System. *J. Chem. Soc., Chem. Commun.* **1994**, *7*, 801−802.

(11) Khan, M. S.; Vishakante, G. D.; Siddaramaiah, H. Gold Nanoparticles: A Paradigm Shift in Biomedical Applications. *Adv. Colloid Interface Sci.* **2013**, *199−200*, 44−58.

(12) Geim, A. K.; Novoselov, K. S. The Rise of Graphene. *Nat. Mater.* **2007**, *6*, 183−191.

(13) Avouris, P.; Chen, Z. H.; Perebeinos, V. Carbon-based Electronics. *Nat. Nanotechnol.* **2007**, *2*, 605−615.

(14) Kang, X. H.; Wang, J.; Wu, H.; Aksay, I. A.; Liu, J.; Lin, Y. H. Glucose Oxidase−Graphene−Chitosan Modified Electrode for Direct Electrochemistry and Glucose Sensing Biosens. *Biosens. Bioelectron.* **2009**, *25*, 901−905.

(15) Schedin, F.; Geim, A. K.; Morozov, S. V.; Hill, E. W.; Blake, P.; Katsnelson, M. I.; Novoselov, K. S. Detection of Individual Gas Molecules Adsorbed on Graphene. *Nat. Mater.* **2007**, *6*, 652−655.

(16) Zhang, D.; Xie, F. X.; Lin, P.; Choy, W. H. Al-TiO2 Composite-Modified Single-Layer Graphene as an Efficient Transparent Cathode for Organic Solar Cells. *ACS Nano* **2013**, *7*, 1740−1747.

(17) Choi, B. G.; Park, H. S. Controlling Size, Amount, and Crystalline Structure of Nanoparticles Deposited on Graphenes for Highly Efficient Energy Conversion and Storage. *ChemSusChem* **2012**, *5*, 709−715.

(18) Bao, H. Q.; Pan, Y. Z.; Ping, Y.; Sahoo, N. G.; Wu, T. F.; Li, L.; Li, J.; Gan, L. H. Chitosan-Functionalized Graphene Oxide as a Nanocarrier for Drug and Gene Delivery. *Small* **2011**, *7*, 1569−1578.

(19) Guo, Y. J.; Guo, S. J.; Ren, J. T.; Zhai, Y. M.; Dong, S. J.; Wang, E. K. Cyclodextrin Functionalized Graphene Nanosheets with High Supramolecular Recognition Capability: Synthesis and HostGuest Inclusion for Enhanced Electrochemical Performance. *ACS Nano* **2010**, *4*, 4001−4010.

(20) Dimiev, A.; Kosynkin, D. V.; Slesarev, A.; Sun, Z.; Tour, J. M. Layer-by-Layer Removal of Graphene for Device Patterning. *Science* **2011**, *331*, 1168−1172.

(21) Tao, C. A.; Wang, J. F.; Qin, S. Q.; Lv, Y. N.; Long, Y.; Zhu, H.; Jiang, Z. H. Fabrication of pH-Sensitive Graphene Oxide−Drug

Supramolecular Hydrogels as Controlled Release Systems. *J. Mater. Chem.* **2012**, *22*, 24856−24861.

(22) Lim, D.-K.; Barhoumi, A.; Wylie, R. G.; Reznor, G.; Langer, R. S.; Kohane, D. S. Enhanced Photothermal Effect of Plasmonic Nanoparticles Coated with Reduced Graphene Oxide. *Nano Lett.* **2013**, *13*, 4075−4079.

(23) Tao, C. A.; Wang, J. F.; Lv, Y. N.; Long, Y.; Zhu, H.; Jiang, Z. H. In Situ Fabrication of pH-Sensitive Graphene Oxide−Drug Supramolecular Hydrogels as Controlled Release System. *J. Controlled Release* **2013**, *172*, e21.

(24) Nergiz, S. Z.; Gandra, N.; Tadepalli, S.; Singamaneni, S. Multifunctional Hybrid Nanopatches of Graphene Oxide and Gold Nanostars for Ultraefficient Photothermal Cancer Therapy. *ACS Appl. Mater. Interfaces* **2014**, *6*, 16395−16402.

(25) Bian, X.; Song, Z. L.; Qian, Y.; Gao, W.; Cheng, Z. Q.; Chen, L.; Liang, H.; Ding, D.; Nie, X. K.; Chen, Z.; Tan, W. H. Fabrication of Graphene-Isolated-Au-Nanocrystal Nanostructures for Multimodal Cell Imaging and Photothermal-Enhanced Chemotherapy. *Sci. Rep.* **2014**, *4*, 6093.

(26) Chen, Y. T.; Guo, F.; Qiu, Y.; Hu, H.; Kulaots, I.; Walsh, E.; Hurt, R. H. Encapsulation of Particle Ensembles in Graphene Nanosacks as a New Route to Multifunctional Materials. *ACS Nano* **2013**, *7*, 3744−3753.

(27) Chen, Y. T.; Guo, F.; Jachak, A.; Kim, S.-P.; Datta, D.; Liu, J. Y.; Kulaots, I.; Vaslet, C.; Jang, H. D.; Huang, J. X.; Kane, A.; Shenoy, V. B.; Hurt, R. H. Aerosol Synthesis of Cargo-Filled Graphene Nanosacks. *Nano Lett.* **2012**, *12*, 1996−2002.

(28) Lin, D.; Qin, T.; Wang, Y.; Sun, X.; Chen, L. Graphene Oxide Wrapped SERS Tags: Multifunctional Platforms toward Optical Labeling, Photothermal Ablation of Bacteria, and the Monitoring of Killing Effect. *ACS Appl. Mater. Interfaces* **2014**, *6*, 1320−1329.

(29) Xu, C.; Yang, D. R.; Mei, L.; Lu, B. G.; Chen, L. B.; Li, Q. H.; Zhu, H. Z.; Wang, T. H. Encapsulating Gold Nanoparticles or Nanorods in Graphene Oxide Shells as a Novel Gene Vector. *ACS Appl. Mater. Interfaces* **2013**, *5*, 2715−2724.

(30) Xu, C.; Yang, D. R.; Mei, L.; Li, Q.; Zhu, H.; Wang, T. Targeting Chemophotothermal Therapy of Hepatoma by Gold Nanorods/Graphene Oxide Core/Shell Nanocomposites. *ACS Appl. Mater. Interfaces* **2013**, *5*, 12911−12920.

(31) Richardson, J. J.; Bjornmalm, M.; Caruso, F. Technology-Driven Layer-by-Layer Assembly of Nanofilms. *Science* **2015**, *348*, aaa2491.

(32) Borges, J.; Mano, J. F. Molecular Interactions Driving the Layer-by-Layer Assembly of Multilayers. *Chem. Rev.* **2014**, *114*, 8883−8942.

(33) Cheng, M. J.; Shi, F.; Li, J. S.; Lin, Z. F.; Jiang, C.; Xiao, M.; Zhang, L. Q.; Yang, W. T.; Nishi, T. Macroscopic Supramolecular Assembly of Rigid Building Blocks through a Flexible Spacing Coating. *Adv. Mater.* **2014**, *26*, 3009−3013.

(34) Cheng, M. J.; Jiang, C.; Ding, J. Y.; Zhang, Y. J.; Fu, Y.; Shi, F. Layer-by-Layer Self-Assembly and Disassembly of Single Charged Inorganic Small Molecules: Towards Surface Patterning. *Phys. Chem. Chem. Phys.* **2013**, *15*, 15172−15176.

(35) Tao, C. A.; An, Q.; Zhu, W.; Yang, H. W.; Li, W. N.; Lin, C. X.; Xu, D.; Li, G. T. Cucurbit[n]urils as a SERS Hot-Spot Nanocontainer through Bridging Gold Nanoparticles. *Chem. Commun.* **2011**, *47*, 9867−9869.

(36) Xu, L. N.; Lv, F. Z.; Zhang, Y. H.; Luan, X. L.; Zhang, Q.; An, Q. Interfacial Modification of Magnetic Montmorillonite (MMT) Using Covalently Assembled LbL Multilayers. *J. Phys. Chem. C* **2014**, *118*, 20357−20362.

(37) Guo, X. H.; Hu, N. F. Increment of Density of Au Nanoparticles Deposited in Situ within Layer-by-Layer Films and Its Enhancement on the Electrochemistry of Ferrocenecarboxylic Acid and Bioelectrocatalysis. *J. Phys. Chem. C* **2009**, *113*, 9831−9837.

(38) Tan, Y. N.; Lee, J. Y.; Wang, D. I. C. Morphosynthesis of Gold Nanoplates in Polypeptide Multilayer Films. *J. Phys. Chem. C* **2009**, *113*, 10887−10895.

(39) Lin, L.; Liu, L.; Zhao, B.; Xie, R.; Lin, W.; Li, H.; Li, Y. Y.; Shi, M. L.; Chen, Y. G.; Springer, T. A.; Chen, X. Carbon Nanotube-Assisted Optical Activation of TGF-β Signalling by Near-Infrared Light. *Nat. Nanotechnol.* **2015**, *10*, 465−471.

(40) Riedinger, A.; Guardia, P.; Curcio, A.; Garcia, M. A.; Cingolani, R.; Manna, L.; Pellegrino, T. Subnanometer Local Temperature Probing and Remotely Controlled Drug Release Based on Azo-Functionalized Iron Oxide Nanoparticles. *Nano Lett.* **2013**, *13*, 2399−2406.

(41) Chakravarty, P.; Marches, R.; Zimmerman, N. S.; Swafford, A. D.-E.; Bajaj, P.; Musselman, I. H.; Pantano, P.; Draper, R. K.; Vitetta, E. S. Thermal Ablation of Tumor Cells with Antibody-Functionalized Single-Walled Carbon Nanotubes. *Proc. Natl. Acad. Sci. U. S. A.* **2008**, *105*, 8697−8702.

(42) Shang, L.; Wang, Y. L.; Huang, L. J.; Dong, S. J. Preparation of DNA-Silver Nanohybrids in Multilayer Nanoreactors by in Situ Electrochemical Reduction, Characterization, and Application. *Langmuir* **2007**, *23*, 7738−7744.

(43) Tiwari, V. S.; Oleg, T.; Darbha, G. K.; Hardy, W.; Singh, J. P.; Ray, P. C. Non-Resonance SERS Effects of Silver Colloids with Different Shapes. *Chem. Phys. Lett.* **2007**, *446*, 77−82.

(44) Yao, H. Q.; Jin, L.; Sue, H. J.; Sumi, Y.; Nishimura, R. Facile Decoration of Au Nanoparticles on Reduced Graphene Oxide Surfaces via a One-Step Chemical Functionalization Approach. *J. Mater. Chem. A* **2013**, *1*, 10783−10789.

(45) Chen, S. N.; Li, X.; Zhao, Y. Y.; Chang, L. M.; Qi, J. Y. Graphene Oxide Shell-Isolated Ag Nanoparticles for Surface-Enhanced Raman Scattering. *Carbon* **2015**, *81*, 767−772.

(46) Song, E.; Han, W. Y.; Li, C.; Cheng, D.; Li, L. R.; Liu, L. C.; Zhu, G. Z.; Song, Y.; Tan, W. H. Hyaluronic Acid-Decorated Graphene Oxide Nanohybrids as Nanocarriers for Targeted and pH-Responsive Anticancer Drug Delivery. *ACS Appl. Mater. Interfaces* **2014**, *6*, 11882−11890.